Nonlocal regularization of sharp-crack energetics: a variational bridge from Griffith geometry to emergent constitutive degradation

Yuqi Sun

School of Mathematical Sciences, Key Laboratory of Intelligent Computing and Applications (Ministry of Education), Tongji University, Shanghai, 200092, China

Abstract

We develop a nonlocal diffusive crack model with displacement as the sole primary field and no independent fracture order parameter. A bounded saturation potential regularizes a spatially averaged elastic strain-energy measure. Under the stated assumptions, an established nonlocal approximation theorem yields rigorous Γ-convergence of the corresponding unsplit reference energy to the Griffith energy as the regularization length vanishes. The small-energy slope and saturation level recover the bulk elastic energy and fracture-energy coefficient, respectively. Exact first variation gives a nonlocal stress modulated by the adjoint average of the saturation derivative. For smooth, nondecreasing, concave potentials, this derivative decreases monotonically from unity to zero, emerging as a degradation function without being prescribed independently. Potentials sharing the same Griffith limit can nevertheless produce different finite-scale stress responses and homogeneous peak strengths. The formulation thus links sharp-crack energetics and constitutive degradation through a single displacement-based energy.

Keywords: nonlocal regularization, variational fracture, Γ-convergence, emergent constitutive degradation, adaptive finite elements

Email address: yuqisun@tongji.edu.cn (Yuqi Sun)

1. Introduction

Fracture couples solid deformation to the creation of an internal surface. Griffith's energetic description balances elastic-energy release against the surface-creation cost [1]. Variational fracture treats displacement and crack geometry as unknowns [2, 3], allowing crack paths to emerge from energetic competition. The resulting difficulty is to represent displacement jumps across an evolving surface. Enriched finite elements accommodate these jumps without a crack-conforming mesh, but retain an explicit crack geometry [4].

Diffusive fracture methods replace the sharp surface with a distributed energy. Building on elliptic approximations of free-discontinuity functionals [5], phase-field fracture couples displacement to a scalar crack field [6]. Subsequent developments address unilateral effects [7], staggered solution schemes [8], and alternative formulations [9]. Crack-density and degradation functions prescribe the geometric and constitutive coupling, while cohesive formulations accommodate opening-dependent responses [10, 11]. These approaches describe complex crack patterns without explicitly tracking their surfaces, at the cost of introducing an auxiliary fracture field.

Nonlocal and gradient-enhanced damage models introduce spatial scales to regularize softening and localization [12, 13], and variational gradient damage connects these processes to brittle-fracture energetics [14]. Other routes include peridynamic integral interactions [15] and nonlocal cohesive potentials with brittle limits [16]. Eliminating a local damage variable can also produce a saturating effective energy [17]. Can we develop a variational diffusive crack model grounded in sharp-crack energetics, with displacement as its sole primary variable?

The mathematical foundation is provided by nonlocal approximations of free-discontinuity energies, beginning with the scalar construction of Braides and Dal Maso [18]. For finite-element fracture energies, Lussardi and Negri [19] combined nonlocal averaging with saturation, established a Griffith-type Γ-limit, and derived the associated nonlocal stress by variation. Their formulation uses the unsplit elastic energy and does not distinguish tension from compression. Scilla and Solombrino [20] established Γ-convergence of saturating, ball-averaged strain-energy functionals to Griffith energy for vector displacements in a generalized bounded-deformation setting [21, 22]. Building on this framework, we saturate only the nonlocal tensile energy while retaining the compressive contribution locally. This split prevents compressive strain concentrations from benefiting from energy saturation and is central

to the mechanical response studied here.

The central connection is that one saturation potential controls both sharp-crack energetics and finite-scale constitutive degradation. Its small-energy slope and saturation level calibrate the limiting bulk and surface energies. Exact variation yields a stress coefficient through adjoint averaging of its derivative. For smooth, nondecreasing, concave potentials, this derivative has the familiar monotone attenuation properties of a degradation function [14, 10], without an independently prescribed degradation law. A homogeneous uniaxial analysis further shows how the potential shape and nonlocal length set the peak-stress scale. Two benchmarks of dynamic fracture are considered on the basis of an adaptive finite-element discretization.

Section 2 introduces the split model, derives its governing equations, and examines its sharp-interface consistency. Section 3 examines the connection between Griffith energetics and constitutive degradation. Section 4 outlines the numerical implementation and presents two dynamic benchmarks: crack branching and the Kalthoff–Winkler impact test.

2. Variational governing equations and sharp-interface consistency

Starting from the Griffith energy, we formulate a displacement-only model that saturates the nonlocal tensile energy and retains the compressive energy locally. We then derive its stress and governing equations for fracture, and examine its sharp-interface consistency.

2.1. The Griffith energy of sharp cracks

Let $\Omega \subset \mathbb{R}^d$ be a bounded open set, $d \geq 2$, and let $\mathbf{u} : \Omega \to \mathbb{R}^d$ denote the displacement field. For a displacement field, the infinitesimal strain is

$$\mathbf{e}(\mathbf{u}) = \mathrm{sym}\nabla\mathbf{u} = \frac{1}{2}\big(\nabla\mathbf{u} + (\nabla\mathbf{u})^{\mathsf{T}}\big). \tag{1}$$

The jump set $J_{\mathbf{u}}$ of the displacement field is defined through its one-sided approximate limits. For $\mathbf{x} \in \Omega$, $\rho > 0$, and $\boldsymbol{\nu} \in \mathbb{S}^{d-1}$, let

$$B_\rho^{\pm}(\mathbf{x}, \boldsymbol{\nu}) := \big\{\mathbf{y} \in B_\rho(\mathbf{x}) : \ \pm(\mathbf{y} - \mathbf{x}) \cdot \boldsymbol{\nu} > 0\big\}. \tag{2}$$

Then

$$\begin{aligned} J_{\mathbf{u}} := \Big\{&\mathbf{x} \in \Omega : \ \exists\, \mathbf{u}^{\pm}(\mathbf{x}) \in \mathbb{R}^d,\ \boldsymbol{\nu}_{\mathbf{u}}(\mathbf{x}) \in \mathbb{S}^{d-1},\ \mathbf{u}^{+}(\mathbf{x}) \neq \mathbf{u}^{-}(\mathbf{x}), \\ &\lim_{\rho \downarrow 0} \fint_{B_\rho^{\pm}(\mathbf{x}, \boldsymbol{\nu}_{\mathbf{u}}(\mathbf{x}))} \big(1 \wedge |\mathbf{u}(\mathbf{y}) - \mathbf{u}^{\pm}(\mathbf{x})|\big)\, \mathrm{d}\mathbf{y} = 0\Big\}. \end{aligned} \tag{3}$$

Here $\mathbf{u}^{\pm}$ are the one-sided approximate traces, $\boldsymbol{\nu}_{\mathbf{u}}$ is the measure-theoretic unit normal, and $[\![\mathbf{u}]\!] := \mathbf{u}^{+} - \mathbf{u}^{-}$ is the displacement jump. The triple $(\mathbf{u}^{+}, \mathbf{u}^{-}, \boldsymbol{\nu}_{\mathbf{u}})$ is determined up to the simultaneous interchange of $+$ and $-$ and reversal of the normal.

The total potential including the Griffith crack energy is defined by

$$\Pi_0[\mathbf{u}] = \int_{\Omega \setminus J_{\mathbf{u}}} W(\mathbf{e}(\mathbf{u}))\, \mathrm{d}\mathbf{x} + G_c \mathcal{H}^{d-1}(J_{\mathbf{u}}) - \ell_{\mathrm{ext}}[\mathbf{u}], \tag{4}$$

where W is the elastic strain-energy density functional, $G_c > 0$ is the critical energy-release rate, $\ell_{\mathrm{ext}}[\mathbf{u}]$ is the external loading potential, and $\mathcal{H}^{d-1}(J_{\mathbf{u}})$ is the Hausdorff measure of the sharp-crack interface.

The natural variational setting of (4) is $GSBD^p(\Omega)$ rather than a classical Sobolev space. Here $GSBD^p(\Omega)$ denotes the space of generalized special functions of bounded deformation whose approximate symmetric gradient belongs to $L^p(\Omega)$ and whose jump set has finite $\mathcal{H}^{d-1}$-measure; unlike a Sobolev space, it admits displacement jumps across rectifiable hypersurfaces [21]. The central difficulty in (4) is geometric: the lower-dimensional set $J_{\mathbf{u}}$ is itself an unknown component of the minimization problem [1, 2].

The objective here is to regularize the sharp-crack energy while retaining the displacement field $\mathbf{u}$ as the only primary field. In particular, no explicit crack geometry, phase field, or independently postulated damage variable is introduced. The jump set $J_{\mathbf{u}}$ appears only in the limiting description; at finite scale, it is neither explicitly tracked nor treated as an independent unknown.

2.2. Nonlocal regularization with a tension–compression split

For isotropic elasticity, write

$$W(\mathbf{e}) = \frac{\lambda}{2}(\operatorname{tr}\mathbf{e})^2 + \mu\, \mathbf{e} : \mathbf{e}, \tag{5}$$

where λ and μ are Lamé parameters. Following the strain-spectral decomposition [8], define

$$\mathbf{e} = \sum_{\alpha=1}^{d} \eta_\alpha \mathbf{n}_\alpha \otimes \mathbf{n}_\alpha, \quad \mathbf{e}^{\pm} = \sum_{\alpha=1}^{d} \langle \eta_\alpha \rangle_{\pm} \mathbf{n}_\alpha \otimes \mathbf{n}_\alpha. \tag{6}$$

where $\langle r \rangle_+ = \max(r, 0)$ and $\langle r \rangle_- = \min(r, 0)$. Thus, the elastic energy can be decomposed as

$$W(\mathbf{e}) = W^{+}(\mathbf{e}) + W^{-}(\mathbf{e}), \tag{7}$$

where $W^{\pm}(\mathbf{e}) = \frac{\lambda}{2}\langle \operatorname{tr}\mathbf{e}\rangle_{\pm}^2 + \mu\,\mathbf{e}^{\pm} : \mathbf{e}^{\pm}$.

For a scalar field f, define the normalized ball average

$$(\mathcal{A}_\varepsilon f)(\mathbf{x}) = \frac{1}{m_\varepsilon(\mathbf{x})}\int_{B_\varepsilon(\mathbf{x})\cap\Omega} f(\mathbf{y})\,\mathrm{d}\mathbf{y}, \tag{8}$$

where $m_\varepsilon(\mathbf{x}) = |B_\varepsilon(\mathbf{x})\cap\Omega|$ and $\varepsilon > 0$ is the interaction radius. The lower-semicontinuous, nondecreasing saturation potential $\Phi : [0,\infty) \to [0,\infty)$ satisfies

$$\Phi(0) = 0, \quad \lim_{s\downarrow 0}\frac{\Phi(s)}{s} = 1, \quad \lim_{s\to\infty}\Phi(s) = \frac{G_c}{2}. \tag{9}$$

We use the exponential potential

$$\Phi_{\exp}(s) = \frac{G_c}{2}\left(1 - \exp\left[-\frac{2s}{G_c}\right]\right). \tag{10}$$

Alternative potentials are listed in Appendix A. The tensile nonlocal energy measure and the split stored energy are

$$\mathcal{F}_\varepsilon^{\mathrm{split}}[\mathbf{u}] = \int_\Omega W^-(\mathbf{e}(\mathbf{u}))\,\mathrm{d}\mathbf{x} + \frac{1}{\varepsilon}\int_\Omega \Phi(s_\varepsilon^+[\mathbf{u}])\,\mathrm{d}\mathbf{x}. \tag{11}$$

where $s_\varepsilon^+[\mathbf{u}] = \varepsilon\mathcal{A}_\varepsilon[W^+(\mathbf{e}(\mathbf{u}))]$. The compressive energy is neither averaged nor saturated. Thus tensile localization can reduce the tensile load-carrying capacity, whereas compressive energy remains unbounded under increasing compressive strain.

Let Ω be a fixed Lipschitz reference domain, with disjoint Dirichlet and Neumann boundary parts Γ_D and Γ_N. For physical time $t \in [0,T]$, impose $\mathbf{u} = \bar{\mathbf{u}}(t)$ on Γ_D and define

$$\Pi_\varepsilon^{\mathrm{split}}[\mathbf{u};t] = \mathcal{F}_\varepsilon^{\mathrm{split}}[\mathbf{u}] - \ell_{\mathrm{ext}}(t)[\mathbf{u}], \tag{12}$$

where the prescribed body force per unit reference volume $\mathbf{b}$ and traction $\bar{\mathbf{t}}$ give

$$\ell_{\mathrm{ext}}(t)[\mathbf{u}] = \int_\Omega \mathbf{b}(\mathbf{x},t)\cdot\mathbf{u}\,\mathrm{d}\mathbf{x} + \int_{\Gamma_N}\bar{\mathbf{t}}(\mathbf{x},t)\cdot\mathbf{u}\,\mathrm{d}a. \tag{13}$$

2.3. Energy variations

The integral kernel of (8) is $K_\varepsilon(\mathbf{x},\mathbf{y}) = \frac{\mathbf{1}_{\{|\mathbf{x}-\mathbf{y}|<\varepsilon\}}}{m_\varepsilon(\mathbf{x})}$. Accordingly, the adjoint of the averaging operator is

$$(\mathcal{A}_\varepsilon^* g)(\mathbf{y}) = \int_{B_\varepsilon(\mathbf{y})\cap\Omega}\frac{g(\mathbf{x})}{m_\varepsilon(\mathbf{x})}\,\mathrm{d}\mathbf{x}. \tag{14}$$

In general, $\mathcal{A}_\varepsilon^* \neq \mathcal{A}_\varepsilon$ because the normalization depends on the centre $\mathbf{x}$ of the truncated ball.

Proposition 2.1 (Variationally consistent split stress)**.** *Let* $\mathbf{u}$ *be an admissible displacement and* $\mathbf{v}$ *an admissible variation, with* $\mathbf{u}, \mathbf{v} \in W^{1,p}(\Omega;\mathbb{R}^d)$, $p>1$, *and let* $\mathbf{v}=\mathbf{0}$ *on* Γ_D. *Assume that* $W^\pm : \mathbb{R}^{d\times d}_{\mathrm{sym}} \to [0,\infty)$ *are* C^1 *and*

$$|D_{\mathbf{E}} W^\pm(\mathbf{E})| \le C_W(1+|\mathbf{E}|^{p-1}) \quad \textit{for all } \mathbf{E}\in\mathbb{R}^{d\times d}_{\mathrm{sym}}, \tag{15}$$

that $\Phi \in C^1([0,\infty))$ *has bounded derivative, and that* ℓ_{ext} *is differentiable at* $\mathbf{u}$. *Define*

$$\boldsymbol{\sigma}^\pm(\mathbf{u}) = D_{\mathbf{E}} W^\pm(\mathbf{e}(\mathbf{u})), \quad q_\varepsilon^+[\mathbf{u}](\mathbf{x}) = \Phi'\big(s_\varepsilon^+[\mathbf{u}](\mathbf{x})\big), \tag{16}$$

and

$$a_\varepsilon^+[\mathbf{u}](\mathbf{y}) = (\mathcal{A}_\varepsilon^* q_\varepsilon^+[\mathbf{u}])(\mathbf{y}). \tag{17}$$

Then

$$D\Pi_\varepsilon^{\mathrm{split}}[\mathbf{u};t](\mathbf{v}) = \int_\Omega \big(\boldsymbol{\sigma}^-(\mathbf{u}) + a_\varepsilon^+[\mathbf{u}]\boldsymbol{\sigma}^+(\mathbf{u})\big) : \mathbf{e}(\mathbf{v})\,\mathrm{d}\mathbf{y} - \ell_{\mathrm{ext}}(t)[\mathbf{v}], \tag{18}$$

and the variationally consistent stress is

$$\boldsymbol{\sigma}_\varepsilon^{\mathrm{split}} = \boldsymbol{\sigma}^- + a_\varepsilon^+\boldsymbol{\sigma}^+, \quad \boldsymbol{\sigma}^\pm = \lambda\langle \operatorname{tr}\mathbf{e}\rangle_\pm \mathbf{I} + 2\mu\mathbf{e}^\pm \tag{19}$$

for (6).

Proof. The directional derivative of the tensile nonlocal energy measure is

$$Ds_\varepsilon^+[\mathbf{u}](\mathbf{v}) = \varepsilon\mathcal{A}_\varepsilon\big[\boldsymbol{\sigma}^+(\mathbf{u}) : \mathbf{e}(\mathbf{v})\big]. \tag{20}$$

The chain rule and cancellation of the prefactor $1/\varepsilon$ give

$$D\mathcal{F}_\varepsilon^{\mathrm{split}}[\mathbf{u}](\mathbf{v}) = \int_\Omega \boldsymbol{\sigma}^- : \mathbf{e}(\mathbf{v})\,\mathrm{d}\mathbf{x} + \int_\Omega q_\varepsilon^+[\mathbf{u}]\,\mathcal{A}_\varepsilon\big[\boldsymbol{\sigma}^+(\mathbf{u}) : \mathbf{e}(\mathbf{v})\big]\,\mathrm{d}\mathbf{x} \tag{21}$$

$$= \int_\Omega \big(\boldsymbol{\sigma}^- + (\mathcal{A}_\varepsilon^* q_\varepsilon^+)\boldsymbol{\sigma}^+\big) : \mathbf{e}(\mathbf{v})\,\mathrm{d}\mathbf{y}, \tag{22}$$

which proves (18). □

For the exponential potential,

$$q_\varepsilon^+ = \exp\left(-\frac{2s_\varepsilon^+}{G_c}\right), \quad a_\varepsilon^+ = \mathcal{A}_\varepsilon^*\left[\exp\left(-\frac{2\varepsilon}{G_c}\mathcal{A}_\varepsilon W^+(\mathbf{e}(\mathbf{u}))\right)\right]. \tag{23}$$

2.4. Elastodynamics

Let $\rho(\mathbf{x}) > 0$ be the reference mass density, define the kinetic energy and action by

$$\mathcal{T}[\dot{\mathbf{u}}] = \frac{1}{2}\int_\Omega \rho|\dot{\mathbf{u}}|^2\,\mathrm{d}\mathbf{x}, \quad \mathcal{S}[\mathbf{u}] = \int_0^T \left(\mathcal{T}[\dot{\mathbf{u}}] - \Pi_\varepsilon^{\mathrm{split}}[\mathbf{u};t]\right)\,\mathrm{d}t. \tag{24}$$

Stationarity of $\mathcal{S}$ for variations vanishing on Γ_D and at the temporal endpoints, followed by integration by parts in time, gives

$$\int_\Omega \rho\ddot{\mathbf{u}}\cdot\mathbf{v}\,\mathrm{d}\mathbf{x} + \int_\Omega \boldsymbol{\sigma}_\varepsilon^{\mathrm{split}} : \mathbf{e}(\mathbf{v})\,\mathrm{d}\mathbf{x} = \ell_{\mathrm{ext}}(t)[\mathbf{v}] \quad \text{for all } \mathbf{v} = \mathbf{0} \text{ on } \Gamma_D. \tag{25}$$

For sufficiently regular solutions, the initial–boundary-value problem is

$$\begin{cases} \rho\ddot{\mathbf{u}} = \operatorname{div}\boldsymbol{\sigma}_\varepsilon^{\mathrm{split}} + \mathbf{b} & \text{in } \Omega\times(0,T),\\ \mathbf{u} = \bar{\mathbf{u}}(t) & \text{on } \Gamma_D\times(0,T),\\ \boldsymbol{\sigma}_\varepsilon^{\mathrm{split}}\mathbf{n} = \bar{\mathbf{t}} & \text{on } \Gamma_N\times(0,T),\\ \mathbf{u}(\mathbf{x},0) = \mathbf{u}_0(\mathbf{x}),\ \dot{\mathbf{u}}(\mathbf{x},0) = \mathbf{v}_0(\mathbf{x}) & \text{in } \Omega. \end{cases} \tag{26}$$

Here $\mathbf{n}$ is the outward normal and the initial data satisfy the Dirichlet compatibility conditions. For a two-dimensional plate of constant thickness t_p, the stored energy, kinetic energy and external work are multiplied consistently by t_p.

2.5. Sharp-interface consistency and its scope

For comparison with the split model, introduce the unsplit reference energy

$$\mathcal{F}_\varepsilon[\mathbf{u}] = \frac{1}{\varepsilon}\int_\Omega \Phi(s_\varepsilon[\mathbf{u}])\,\mathrm{d}\mathbf{x}, \quad s_\varepsilon[\mathbf{u}] = \varepsilon\mathcal{A}_\varepsilon[W(\mathbf{e}(\mathbf{u}))]. \tag{27}$$

For the unmodified ball average and a convex bulk density with coercive p-growth ($p > 1$), Scilla and Solombrino [20, Theorem 3.1] establish its Griffith limit under the hypotheses stated there. The normalization (9) then gives, in the strong L^1 topology,

$$\mathcal{F}_\varepsilon[\mathbf{u}] \xrightarrow{\Gamma(L^1)} F_0[\mathbf{u}] \;= \int_\Omega W(\mathbf{e}(\mathbf{u}))\,\mathrm{d}\mathbf{x} + G_c\mathcal{H}^{d-1}(J_{\mathbf{u}}). \tag{28}$$

The limit is finite on $GSBD^p(\Omega)\cap L^1(\Omega;\mathbb{R}^d)$ and $+\infty$ otherwise.

The tension–compression split preserves the bulk elastic limit. For a fixed smooth displacement with bounded strain,

$$W^-(\mathbf{e}(\mathbf{u})) + \frac{1}{\varepsilon}\Phi\big(\varepsilon\mathcal{A}_\varepsilon W^+(\mathbf{e}(\mathbf{u}))\big) \longrightarrow W^- + W^+ = W(\mathbf{e}(\mathbf{u})). \tag{29}$$

This consistency for a fixed smooth field does not determine the Γ-limit, which must also account for sequences of displacements whose strains concentrate near emerging cracks. Two features of the split functional prevent a direct application of this reference result.

First, the theorem requires the density inside the nonlocal saturation to satisfy a coercive lower bound $W(\mathbf{E}) \geq c|\mathbf{E}|^p$ with $c > 0$. The tensile density W^+ fails this condition: $W^+(-r\mathbf{I}) = 0$ for every $r > 0$, although $|-r\mathbf{I}| > 0$. Hence no constant $c > 0$ can give $c|\mathbf{E}|^p \leq W^+(\mathbf{E})$ for all symmetric strains. Replacing W by W^+ therefore violates a hypothesis of the reference theorem.

Second, the unsaturated local term W^- changes the cost of approximating displacement jumps, so the unsplit theorem cannot be applied directly. For $d \geq 2$, this distinction can be illustrated by approximating a constant displacement jump $\mathbf{a}$ across the planar interface $\mathbf{x}\cdot\mathbf{n} = 0$, where $|\mathbf{n}| = 1$. Consider the continuous transition $\mathbf{u}_\delta(\mathbf{x}) = \mathbf{a}\,\zeta((\mathbf{x}\cdot\mathbf{n})/\delta)$, with ζ smooth and nondecreasing, $\zeta(r) = 0$ for $r \leq -1/2$, and $\zeta(r) = 1$ for $r \geq 1/2$. Here δ is the transition-layer thickness, whereas $\mathbf{a}$ is the relative displacement of its two sides. Setting $s = \mathbf{x}\cdot\mathbf{n}$, differentiation gives

$$\mathbf{e}(\mathbf{u}_\delta) = \frac{\zeta'(s/\delta)}{\delta}\,\mathbf{A}, \quad \mathbf{A} = \mathbf{a}\odot\mathbf{n} := \frac{\mathbf{a}\otimes\mathbf{n} + \mathbf{n}\otimes\mathbf{a}}{2}. \tag{30}$$

To evaluate $W^-(\mathbf{A})$, decompose the jump as $\mathbf{a} = a_n\mathbf{n} + \mathbf{a}_\tau$, with $a_n = \mathbf{a}\cdot\mathbf{n}$ and $\mathbf{a}_\tau\cdot\mathbf{n} = 0$. In an orthonormal frame whose first axis is $\mathbf{n}$ and whose second axis is aligned with $\mathbf{a}_\tau$ (arbitrary tangential direction if $\mathbf{a}_\tau = \mathbf{0}$), $\mathbf{A}$ has the two-dimensional block

$$\mathbf{A}_{(2)} = \begin{pmatrix} a_n & |\mathbf{a}_\tau|/2 \\ |\mathbf{a}_\tau|/2 & 0 \end{pmatrix}, \quad \det(\mathbf{A}_{(2)} - \eta\mathbf{I}) = \eta^2 - a_n\eta - \frac{|\mathbf{a}_\tau|^2}{4}. \tag{31}$$

Any remaining eigenvalues are zero. The two eigenvalues of this block are

$$\eta_\pm = \frac{a_n \pm \sqrt{a_n^2 + |\mathbf{a}_\tau|^2}}{2} = \frac{\mathbf{a}\cdot\mathbf{n} \pm |\mathbf{a}|}{2}, \quad \eta_- \leq 0 \leq \eta_+. \tag{32}$$

Consequently, $\operatorname{tr}\mathbf{A} = \mathbf{a}\cdot\mathbf{n}$ and $\mathbf{A}^- : \mathbf{A}^- = \eta_-^2$. Substitution into the spectral compression energy yields

$$W^-(\mathbf{a}\odot\mathbf{n}) = \frac{\lambda}{2}\langle\mathbf{a}\cdot\mathbf{n}\rangle_-^2 + \frac{\mu}{4}(|\mathbf{a}| - \mathbf{a}\cdot\mathbf{n})^2. \tag{33}$$

Since $\zeta' \geq 0$ and $W^-(c\mathbf{A}) = c^2 W^-(\mathbf{A})$ for $c \geq 0$, the local compressive energy per unit interface area is obtained by integration along the normal direction:

$$\mathcal{E}_\delta^- = \int_{\mathbb{R}} W^-\left(\frac{\zeta'(s/\delta)}{\delta}\mathbf{A}\right) \mathrm{d}s = \frac{C_\zeta}{\delta} W^-(\mathbf{a} \odot \mathbf{n}), \tag{34}$$

where $C_\zeta := \int_{\mathbb{R}} |\zeta'(r)|^2 \, \mathrm{d}r$.

For pure opening, $\mathbf{a} = \gamma\mathbf{n}$ with $\gamma > 0$, this term vanishes. An interior planar opening layer of thickness $\delta_\varepsilon = o(\varepsilon)$ saturates the tensile term in an asymptotic 2ε-wide tube, giving

$$\text{energy per unit opening-interface area} \longrightarrow 2\Phi(\infty) = G_c. \tag{35}$$

For tangential sliding or normal compression, $W^-(\mathbf{a} \odot \mathbf{n}) > 0$, so the local energy of this transition diverges as $\delta \to 0$, unlike pure opening.

Remark 2.2 (Γ-convergence of the split model). A rigorous Γ-convergence analysis of (11) is left for future work. Such an analysis requires identifying the limiting functional, including the admissible displacement jumps and their surface energy, and establishing the corresponding lower bound and matching recovery sequences. The bulk consistency and planar-opening calibration above provide partial consistency checks, but do not determine the full Γ-limit.

3. From Griffith geometry to emergent constitutive degradation

This section uses the unsplit reference energy (27) to clarify how the two endpoint normalizations in (9) simultaneously fix the bulk and surface energies.

3.1. Elastic and Griffith energy limits

The small-s normalization in (9) gives

$$\Phi(s) = s + o(s) \qquad (s \downarrow 0). \tag{36}$$

Hence, at a point where $W(\mathbf{e}(\mathbf{u}))$ is regular and finite,

$$\frac{1}{\varepsilon}\Phi(s_\varepsilon[\mathbf{u}]) = \mathcal{A}_\varepsilon W(\mathbf{e}(\mathbf{u})) + o(1) \longrightarrow W(\mathbf{e}(\mathbf{u})) \quad (\varepsilon \downarrow 0). \tag{37}$$

Thus the unit small-s slope recovers the original elastic energy density. At fixed ε, the nonlocal energy density obeys

$$0 \leq \frac{1}{\varepsilon}\Phi(s_\varepsilon[\mathbf{u}]) \leq \frac{G_c}{2\varepsilon}. \tag{38}$$

To estimate the energy near a crack, consider a smooth crack surface $S \Subset \Omega$ of finite area and define its two-sided tubular neighbourhood by

$$T_\varepsilon(S) := \{\mathbf{x} \in \Omega : \operatorname{dist}(\mathbf{x}, S) < \varepsilon\}. \tag{39}$$

This geometric neighbourhood has thickness 2ε and volume

$$|T_\varepsilon(S)| = 2\varepsilon \mathcal{H}^{d-1}(S) + o(\varepsilon). \tag{40}$$

Consequently, its contribution to the regularized energy satisfies

$$\frac{1}{\varepsilon} \int_{T_\varepsilon(S)} \Phi(s_\varepsilon[\mathbf{u}])\, \mathrm{d}\mathbf{x} \leq \frac{G_c}{2\varepsilon} |T_\varepsilon(S)| = G_c \mathcal{H}^{d-1}(S) + o(1). \tag{41}$$

Thus the energy in this neighbourhood remains bounded even under strain concentration.

The same potential therefore has two complementary asymptotic roles: $\lim_{s\downarrow 0} \Phi(s)/s = 1$ recovers the bulk elastic energy, whereas the saturation level determines the Griffith surface-energy coefficient $2\Phi(\infty) = G_c$, as established by the cited Γ-limit (28) and geometrically illustrated by the crack-layer energy estimate above.

3.2. Emergent degradation and strength

Degradation emerges from the first variation of the nonlocal energy, rather than being prescribed separately at the stress level [19]. Once the saturation potential Φ is specified, variational differentiation determines

$$q(s) = \Phi'(s), \quad \boldsymbol{\sigma}_\varepsilon[\mathbf{u}] = \big(\mathcal{A}_\varepsilon^*[q(s_\varepsilon[\mathbf{u}])]\big)\boldsymbol{\sigma}_0(\mathbf{u}). \tag{42}$$

The function q is therefore an *emergent degradation function*: it is inherited from the energy regularization, rather than introduced as an independent constitutive law. Its action on the elastic stress is transmitted through the adjoint averaging operator.

For a nondecreasing, concave potential $\Phi \in C^1([0,\infty))$ satisfying (9), this variationally induced function automatically satisfies

$$q(0) = 1, \quad 0 \leq q(s) \leq 1, \quad q \text{ is nonincreasing}, \quad \lim_{s\to\infty} q(s) = 0. \tag{43}$$

The unit initial slope fixes $q(0) = 1$, while monotonicity and concavity of Φ imply nonnegativity and monotone decay of q. Its limiting value must vanish,

since a positive limit would contradict the boundedness of Φ. Thus the normalization and decay properties characteristic of a degradation function follow from the saturation potential, rather than being imposed on a separate stress-modulation law.

Since $\Phi(0) = 0$, integration gives

$$\Phi(s) = \int_0^s q(r)\,\mathrm{d}r, \qquad G_c = 2\int_0^\infty q(r)\,\mathrm{d}r. \tag{44}$$

Remark 3.1 (Geometry and emergent degradation). The saturation conditions are introduced to recover the sharp-crack Griffith energy in the Γ-limit. Remarkably, within the smooth concave class considered here, the same energetic structure also generates a degradation function satisfying the physical properties of stress attenuation in (43). Thus, consistency with sharp-crack geometry and the constitutive mechanism of degradation arise from a common variational potential, without prescribing an independent degradation law.

Potentials with the same endpoint normalizations share the Griffith limit but generally yield different finite-scale responses, as the following homogeneous analysis illustrates.

Proposition 3.2 (Homogeneous uniaxial response)**.** *Consider* $W(\eta) = E\eta^2/2$ *under homogeneous uniaxial strain* $\eta \geq 0$*, with* $E > 0$*,* $\varepsilon > 0$*, and* $\Phi \in C^1([0,\infty)) \cap C^2((0,\infty))$*. Set*

$$s = \frac{\varepsilon E \eta^2}{2}, \quad q(s) = \Phi'(s). \tag{45}$$

The energy-conjugate stress along this response is

$$T(\eta) = E\eta\, q(s). \tag{46}$$

Any interior stationary point $s_c > 0$ *of* T *satisfies*

$$\Phi'(s_c) + 2s_c\Phi''(s_c) = 0. \tag{47}$$

Proof. For a homogeneous field, $\mathcal{A}_\varepsilon W = W$ and the energy per unit volume is $\psi_\varepsilon(\eta) = \varepsilon^{-1}\Phi(\varepsilon E\eta^2/2)$. Differentiation gives (46). Since $\mathrm{d}s/\,\mathrm{d}\eta = \varepsilon E\eta = 2s/\eta$,

$$\frac{\mathrm{d}T}{\mathrm{d}\eta} = E\big(\Phi'(s) + 2s\Phi''(s)\big), \tag{48}$$

which yields (47). □

A root of (47) is a peak when the tangent changes from positive to negative. For the concave class satisfying (43), q is nonnegative, nonincreasing, and integrable by (44). Hence $sq(s) \to 0$, and

$$T(s) = \sqrt{\frac{2Es}{\varepsilon}}\, q(s).$$

This stress is positive for sufficiently small $s > 0$ and vanishes at both endpoints, so it attains a positive global maximum. Uniqueness requires an additional condition, define

$$R(s) = -\frac{2sq'(s)}{q(s)}. \tag{49}$$

A unique peak follows if $R(s) < 1$ for $0 < s < s_c$ and $R(s) > 1$ for $s > s_c$ wherever $q(s) > 0$.

For the normalized potentials in table A.4, define the dimensionless peak location $z_c = s_c/G_c$. The homogeneous peak strain and stress can then be written as

$$\eta_c = \sqrt{\frac{2G_c z_c}{\varepsilon E}}, \quad T_c = C_\Phi \sqrt{\frac{EG_c}{\varepsilon}}, \tag{50}$$

where $C_\Phi = \sqrt{2z_c}\,\Phi'(G_c z_c)$ is a dimensionless coefficient determined by the saturation law. The peak locations and coefficients obtained from equation (47) are summarized in table A.5.

For the exponential potential (10),

$$q(s) = \exp\left(-\frac{2s}{G_c}\right), \quad s_c = \frac{G_c}{4}, \quad C_\Phi = \frac{1}{\sqrt{2\mathrm{e}}}, \tag{51}$$

and hence

$$\eta_c = \sqrt{\frac{G_c}{2\varepsilon E}}, \quad T_c = \sqrt{\frac{EG_c}{2\mathrm{e}\,\varepsilon}}. \tag{52}$$

The scaling $T_c \propto \varepsilon^{-1/2}$ shows that, at finite ε, the nonlocal length scale is not merely a numerical smoothing parameter: it sets both the averaging radius and the homogeneous peak-stress scale. For a prescribed T_c on this response,

$$\varepsilon = \frac{C_\Phi^2 E G_c}{T_c^2}. \tag{53}$$

Thus, potentials sharing the same Griffith limit generally predict different homogeneous strengths at fixed (E, G_c, ε).

4. Numerical validation

Two dynamic benchmarks are considered: crack branching and Kalthoff–Winkler impact. Both use adaptive Q_1 meshes and explicit velocity-Verlet integration with lumped mass. Here h_0 is the coarsest element size; the meshes allow up to two refinement levels, with $h_{\min} = h_0/4$. The material data, length-scale parameters and solvers are summarized in Table 1.

Table 1: Material data, length-scale settings and solvers for the two benchmarks. Mesh sizes are rounded for display. Both cases use adaptive meshes with $\varepsilon_K = Mh_K$, with h_K the current cell size.

Quantity	Branching	Kalthoff–Winkler
E (GPa)	32	190
ν	0.20	0.30
G_c (N/mm)	0.003	22.13
Thickness t_p (mm)	1	1
Density ρ (kg/m^3)	2450	8000
Reduction	Plane strain	Plane strain
Mesh size h_0 (mm)	0.667, 0.444, 0.222	1.5, 1, 0.5
Multiplier M	5	3
Radius rule	$\varepsilon_K = 5h_K$	$\varepsilon_K = 3h_K$
Solver	Explicit velocity-Verlet (lumped mass)	Explicit velocity-Verlet (lumped mass)

4.1. Dynamic crack branching

We simulate dynamic crack branching using the geometry, material data and loading of Borden et al. [23]. With the origin at the lower-left corner, the plate and initial slit in Figure 1 are

$$\begin{aligned} \Omega_{\mathrm{B}} &= \big((0,100)\times(0,40)\big)\setminus\Gamma_{0,\mathrm{B}},\\ \Gamma_{0,\mathrm{B}} &= [0,50]\times\{20\}, \end{aligned} \tag{54}$$

with dimensions in millimetres. At $t = 0^+$, equal and opposite 1 MPa tensile tractions are applied to the horizontal edges and held constant; the remaining boundaries are traction-free. The slit faces have independent displacement traces and no cross-slit averaging. Each simulation runs to $80\,\mu$s.

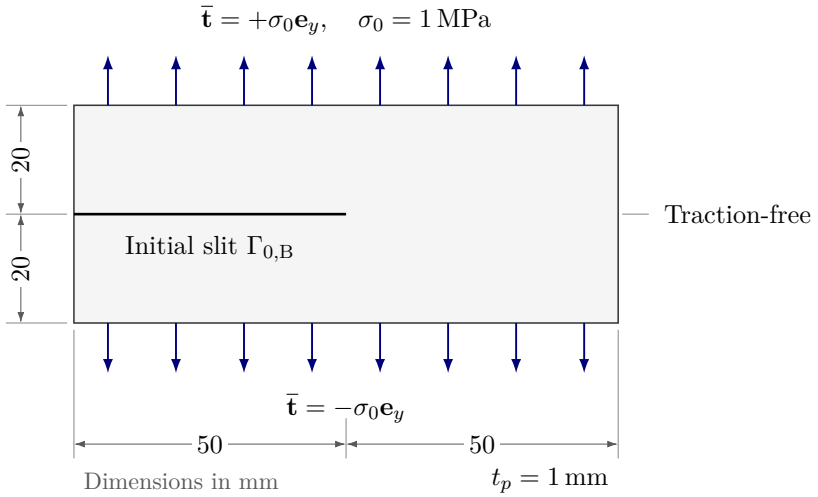

Figure 1: Dynamic branching specimen and step loading.

The three coarse-mesh sizes are $h_0 = 2/3$, $4/9$ and $2/9$ mm. Up to two levels of symmetric refinement are used, with $\varepsilon_K = 5h_K$; the displacement itself is not constrained by symmetry. Both resolution and regularization therefore vary, so this is not a fixed-ε mesh-convergence study.

Figures 2–4 show the fields near $60\,\mu$s: an initially straight crack extension has formed approximately symmetric branches. The indicator band narrows as h_0 decreases, while tensile hydrostatic stress concentrates near the branch tips.

Indicator tracking first resolves parent-crack extension at 15–19 μs and branching at 35.70–37.34 μs. Table 2 shows nearly opposite early branch

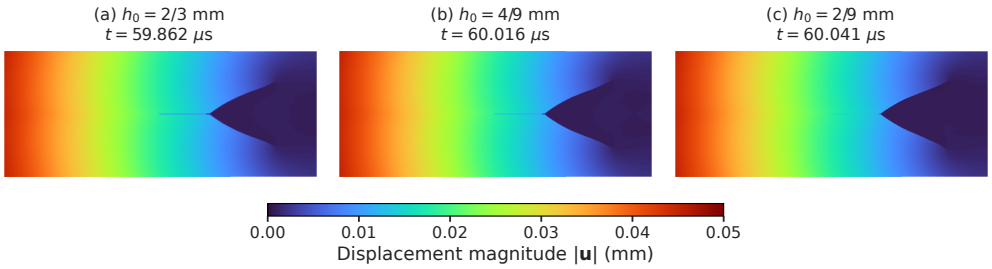

Figure 2: Dynamic branching: displacement magnitude near $60\,\mu$s on the deformed geometry.

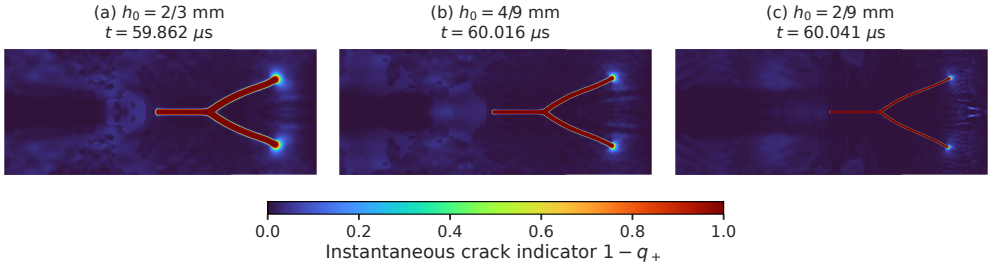

Figure 3: Instantaneous crack indicator $1 - q_+ \in [0, 1]$ for the states in Figure 2.

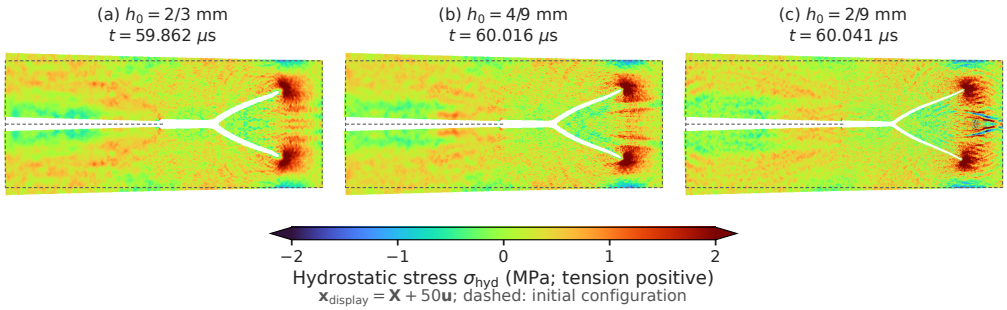

Figure 4: Hydrostatic stress $\sigma_{\mathrm{hyd}} = (\sigma_{xx} + \sigma_{yy} + \sigma_{zz})/3$ for the states in Figure 2. For display, $\mathbf{x} = \mathbf{X} + 50\mathbf{u}$; dashed lines show the initial boundary and notch. Elements with crack indicator $1 - q_+ = 1$ at all four nodes are hidden. The common colour scale is $[-2, 2]$ MPa; exported nodal ranges in panels (a)–(c) are $[-3.26, 2.70]$, $[-5.18, 3.52]$, and $[-7.41, 5.96]$ MPa, respectively. Values outside the colour scale use its endpoint colours.

angles with magnitudes of 27°–31°. These times and angles are threshold-dependent diagnostics; the extraction procedure is given in Appendix B.

Table 2: Dynamic branching: early branch angles.

h_0 (mm)	θ_{upper} (°)	θ_{lower} (°)
2/3	27.34	−27.34
4/9	28.77	−28.77
2/9	30.36	−30.84

Figure 5(a) shows parent-tip speeds reaching about 1.0–1.2 km/s. After branching, the apparent upper-tip speed histories are similar across the three meshes, near 1.1 km/s over 50–60 μs before decreasing. At 80 μs, panel (b) shows modestly higher full split stored energy on finer meshes.

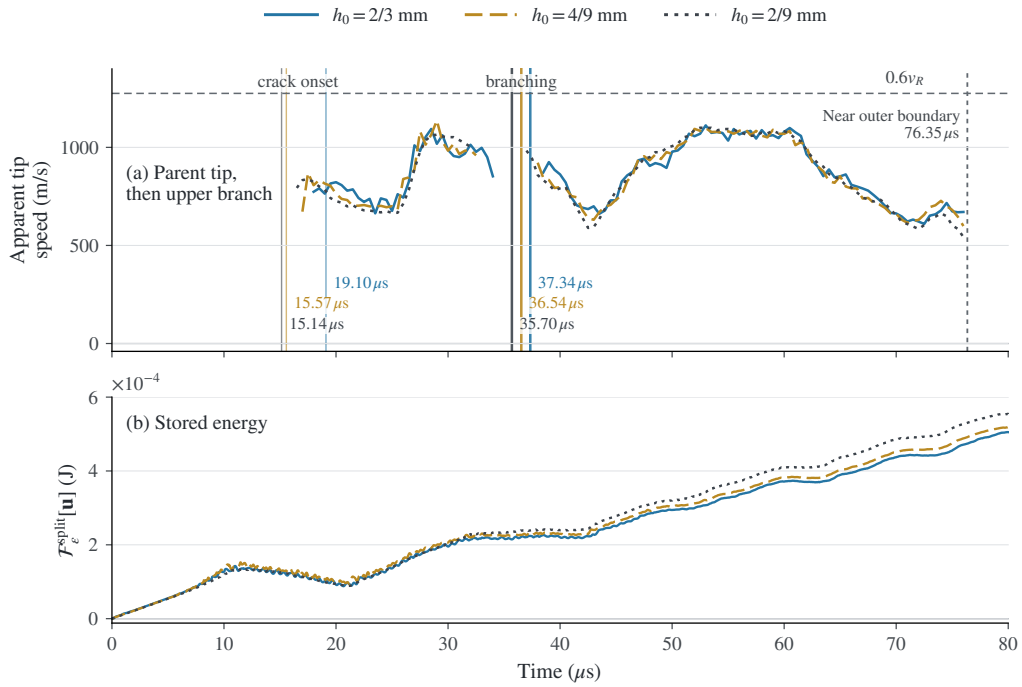

Figure 5: Dynamic branching: (a) apparent tip speed along the parent crack and upper branch; (b) full split stored energy.

4.2. Kalthoff–Winkler impact

This benchmark examines brittle crack kinking under dynamic shear loading [24]. The full plate is modelled, with the loading idealization of Borden et al. [23]. With the origin at the lower-left corner, x horizontal and y vertical, the geometry in Figure 6 is

$$\begin{aligned} \Omega_{\mathrm{KW}} &= \big((0,200)\times(0,100)\big)\setminus(\Gamma_{0,\mathrm{l}}\cup\Gamma_{0,\mathrm{r}}),\\ \Gamma_{0,\mathrm{l}} &= \{75\}\times[50,100], \qquad \Gamma_{0,\mathrm{r}} = \{125\}\times[50,100], \end{aligned} \tag{55}$$

with dimensions in millimetres. A downward velocity is prescribed on the central tongue's upper edge, $\Gamma_v = [75,125]\times\{100\}$:

$$\dot{U}(t) = -\dot{u}_y(t) = v_0 \begin{cases} t/t_r, & 0 \le t \le t_r,\\ 1, & t > t_r, \end{cases} \qquad v_0 = 16.5\ \mathrm{m/s}, \quad t_r = 1\,\mu\mathrm{s}. \tag{56}$$

Here $U(0) = 0$. The horizontal displacement on Γ_v is unconstrained; all remaining boundaries are traction-free. Loading is applied directly to the specimen, without modelling projectile contact. Each simulation runs to $100\,\mu$s.

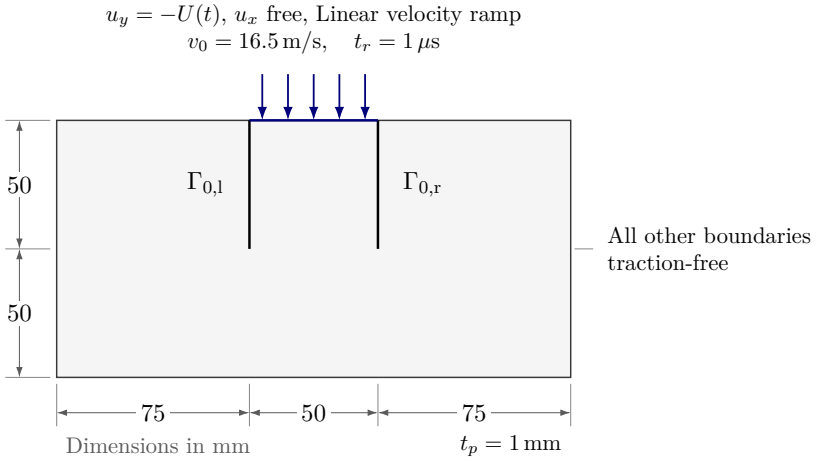

Figure 6: Kalthoff–Winkler geometry and loading. The central tongue is driven by (56); all other boundaries are traction-free.

The results below use $h_0 = 1.5$, 1 and 0.5 mm and $\varepsilon_K = 3h_K$, where h_K is the current cell size. The radius is updated during adaptive refinement, so both resolution and regularization vary.

Figures 7–9 show displacement, crack indicator and hydrostatic stress near 60 μs. All three cases exhibit approximately symmetric outward crack kinking. The indicator bands narrow with decreasing h_0; the coarsest case also shows additional localization at the opposite boundary, $y = 0$.

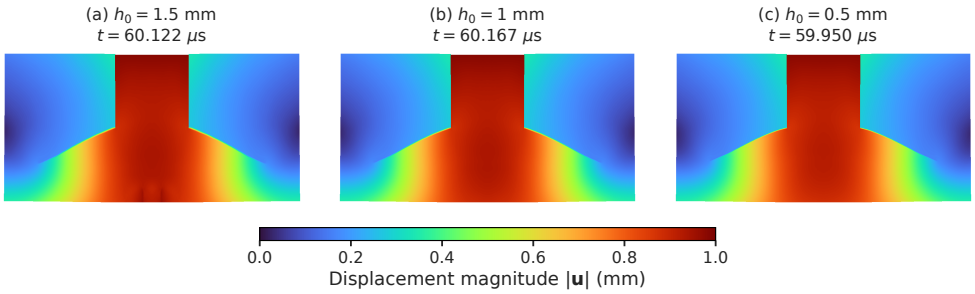

Figure 7: Displacement magnitude near 60 μs on the deformed geometry, oriented as in Figure 6.

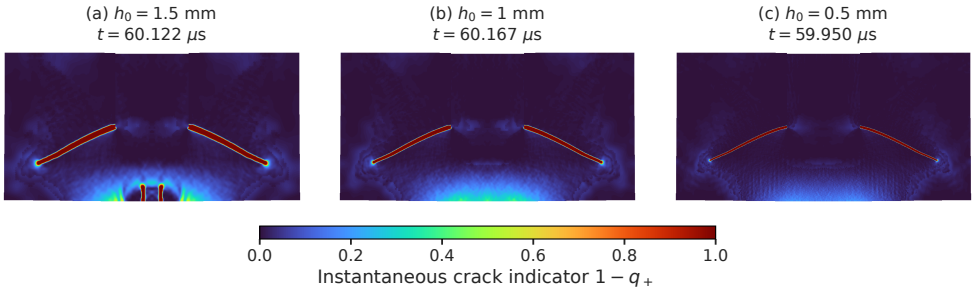

Figure 8: Instantaneous crack indicator $1 - q_+ \in [0, 1]$ for the states in Figure 7.

The indicator first resolves crack extension around 24 μs. Table 3 lists both cracks: negative and positive angles denote clockwise and counterclockwise kinking from the downward initial-slit direction, respectively. Their magnitudes are near the approximately 70° reference [23] and agree to the displayed precision. The extraction procedure is given in Appendix B.

Figure 10(a) shows similar apparent speed histories, reaching approximately 1.6–1.8 km/s over 35–50 μs before decreasing. The near-zero values after about 83 μs coincide with the tips approaching the outer boundaries. Panel (b) compares the full split stored energy in joules, including both the saturated tensile and local compressive contributions.

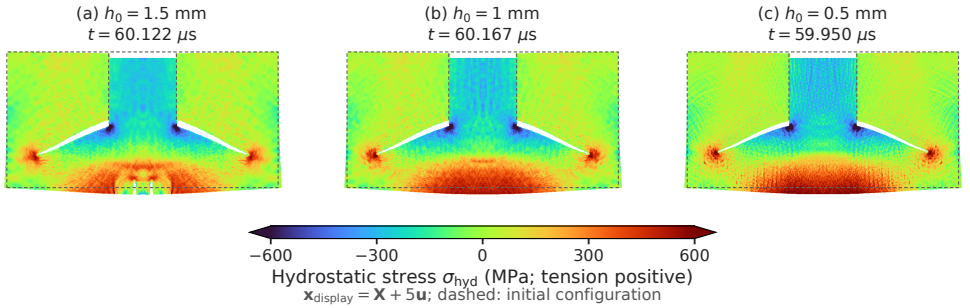

Figure 9: Hydrostatic stress $\sigma_{\mathrm{hyd}} = (\sigma_{xx} + \sigma_{yy} + \sigma_{zz})/3$ for the states in Figure 7. For display, $\mathbf{x} = \mathbf{X} + 5\mathbf{u}$ before the same rigid rotation as in Figure 7; dashed lines show the initial boundary and notches. Elements with crack indicator $1 - q_+ = 1$ at all four nodes are hidden. The common colour scale is $[-600, 600]$ MPa; exported nodal ranges in panels (a)–(c) are $[-1968, 645]$, $[-2417, 721]$, and $[-3261, 1022]$ MPa, respectively. Values outside the colour scale use its endpoint colours.

Table 3: Kalthoff–Winkler: left- and right-tip kink angles.

h_0 (mm)	Left tip θ_{l} (°)	Right tip θ_{r} (°)
1.5	−74.89	+74.89
1	−72.52	+72.52
0.5	−72.65	+72.65

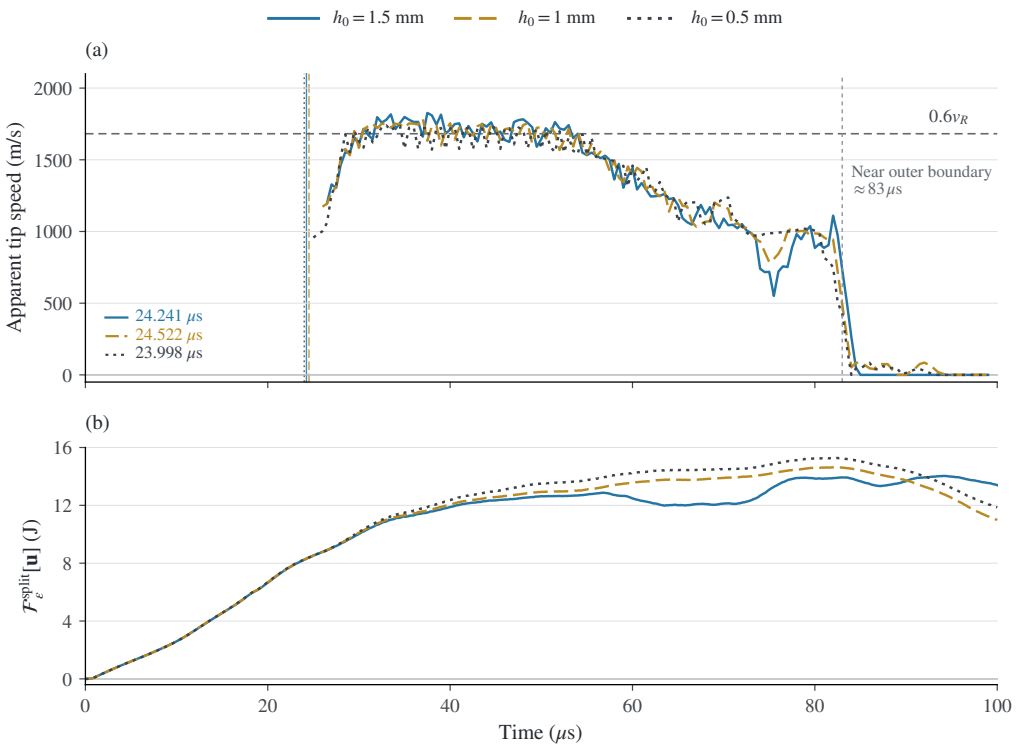

Figure 10: Kalthoff–Winkler impact: (a) apparent right-tip speed; (b) full split stored energy.

5. Conclusions and outlook

We have developed a displacement-only nonlocal variational fracture model that saturates spatially averaged tensile energy while retaining compressive elasticity locally. Exact variation yields a stress whose tensile part is attenuated by the adjoint average of the saturation derivative. Thus neither an auxiliary crack field nor an independently prescribed degradation law is needed. For a smooth, nondecreasing, concave potential, this attenuation decreases monotonically as the nonlocal tensile energy grows.

The potential's small-energy slope recovers intact elasticity, while its saturation level calibrates the Griffith cost of planar opening. The established Griffith Γ-limit applies to the unsplit reference energy; for the proposed split functional, we have shown bulk consistency and planar-opening calibration, but not a full Γ-limit. Even with the same endpoint calibration, the potential shape changes the finite-ε stress response and peak strength.

Two dynamic fracture benchmarks illustrate the model's ability to describe complex crack propagation. Open questions include the sharp-crack limit of the split functional, particularly its admissible jump modes and surface energy, and a systematic analysis of numerical convergence.

Appendix A. Representative saturation potentials

The following normalized potentials all satisfy $\Phi'(0) = 1$ and $\Phi(\infty) = G_c/2$. Their derivatives therefore start from unity and decay to zero, but at different rates.

The finite-cutoff law is C^1 and concave but not C^2 at $s = G_c$. Consequently it satisfies the energetic and monotone stress-modulation conditions, while a classical second derivative should not be used at the cutoff. The different approaches to the common saturation level and the associated decay of q are compared in figure A.11.

The dimensionless peak locations $z_c = s_c/G_c$ and strength coefficients C_Φ in (50), obtained from equation (47), are listed in table A.5.

Appendix B. Crack-path diagnostics and apparent tip speed

Onset, splitting and early angles are diagnosed from the connected Gauss-point set $1 - q_+ \geq 0.95$. Its area-weighted ridge centroids use 0.5 mm radial bins for Kalthoff–Winkler and x-bins for branching. Angles are orthogonal

Table A.4: Representative saturation potentials in the same Griffith Γ-universality class.

Family	$\Phi(s)$	$q(s) = \Phi'(s)$
Exponential	$\dfrac{G_c}{2}\left(1 - e^{-2s/G_c}\right)$	e^{-2s/G_c}
Rational	$\dfrac{s}{1 + 2s/G_c}$	$(1 + 2s/G_c)^{-2}$
Arctangent	$\dfrac{G_c}{\pi}\tan^{-1}\left(\dfrac{\pi s}{G_c}\right)$	$\dfrac{1}{1 + (\pi s/G_c)^2}$
Hyperbolic tangent	$\dfrac{G_c}{2}\tanh\left(\dfrac{2s}{G_c}\right)$	$\operatorname{sech}^2\left(\dfrac{2s}{G_c}\right)$
Finite cutoff	$\begin{cases} s - s^2/(2G_c), & 0 \le s \le G_c, \\ G_c/2, & s > G_c, \end{cases}$	$\max(1 - s/G_c, 0)$

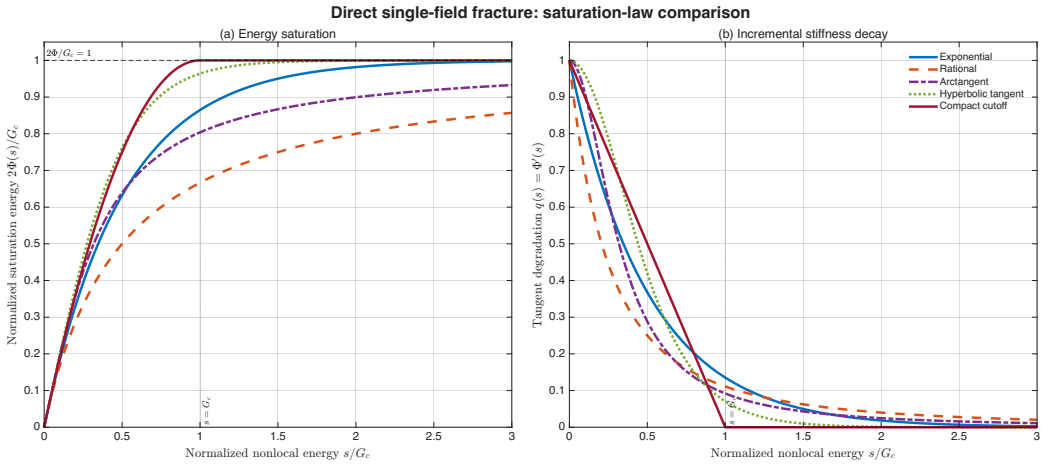

Figure A.11: Comparison of the normalized saturation energy $2\Phi(s)/G_c$ and the associated energetic sensitivity $q(s) = \Phi'(s)$ for the five potentials in table A.4. The vertical dotted line marks $s = G_c$, at which the compact-cutoff potential reaches its plateau and its derivative vanishes.

Table A.5: Homogeneous uniaxial peak locations and strength coefficients in (50) for the potentials in table A.4. For the hyperbolic-tangent potential, z_c is the unique positive root of $8z_c \tanh(2z_c) = 1$.

Family	$z_c = s_c/G_c$	C_Φ
Exponential	$1/4$	$1/\sqrt{2\mathrm{e}} \approx 0.428882$
Rational	$1/6$	$9/(16\sqrt{3}) \approx 0.324760$
Arctangent	$1/(\pi\sqrt{3})$	$\frac{3}{4}\sqrt{2/(\pi\sqrt{3})} \approx 0.454696$
Hyperbolic tangent	≈ 0.260907	$\sqrt{2z_c}\,\operatorname{sech}^2(2z_c) \approx 0.556558$
Finite cutoff	$1/3$	$\sqrt{8/27} \approx 0.544331$

fits 2–8 mm from the initial tip or branch origin, measured counterclockwise from the forward initial-crack direction (downward in Figure 6 for Kalthoff–Winkler). Kalthoff–Winkler speeds use the ridge tip. For branching speeds, the saved nodally projected Q_1 indicator is instead retracked with the same threshold: the initial-tip-connected front gives the parent tip until splitting and the upper-branch tip thereafter. This corrects premature truncation of the original fine-mesh x-bin ridge while retaining the original Gauss-point event and angle diagnostics.

Let $\widehat{\mathbf{r}}(t)$ be the recorded tip position, interpolated within adjacent available states. The plotted apparent speed is

$$v_{\mathrm{app}}(t;\tau) = \frac{\|\widehat{\mathbf{r}}(t+\tau/2) - \widehat{\mathbf{r}}(t-\tau/2)\|}{\tau}, \qquad \tau = 2\,\mu\mathrm{s}, \tag{B.1}$$

at centres spaced by $0.5\,\mu$s. Position and time are converted to metres and seconds before reporting m/s. Endpoints are interpolated only between adjacent saved states; unresolved transitions and contact with the boundary leave gaps.

Declaration of competing interest

The authors declare no known competing financial interests or personal relationships that could have appeared to influence the work reported in this paper.

References

[1] A. A. Griffith, The phenomena of rupture and flow in solids, Philosophical Transactions of the Royal Society of London. Series A 221 (1921) 163–198. doi:10.1098/rsta.1921.0006.

[2] G. A. Francfort, J.-J. Marigo, Revisiting brittle fracture as an energy minimization problem, Journal of the Mechanics and Physics of Solids 46 (1998) 1319–1342. doi:10.1016/S0022-5096(98)00034-9.

[3] B. Bourdin, G. A. Francfort, J.-J. Marigo, The variational approach to fracture, Journal of Elasticity 91 (2008) 5–148. doi:10.1007/s10659-007-9107-3.

[4] N. Moës, J. Dolbow, T. Belytschko, A finite element method for crack growth without remeshing, International Journal for Numerical Methods in Engineering 46 (1999) 131–150. doi:10.1002/(SICI)1097-0207(19990910)46:1<131::AID-NME726>3.0.CO;2-J.

[5] L. Ambrosio, V. M. Tortorelli, Approximation of functionals depending on jumps by elliptic functionals via Γ-convergence, Communications on Pure and Applied Mathematics 43 (1990) 999–1036. doi:10.1002/cpa.3160430805.

[6] B. Bourdin, G. A. Francfort, J.-J. Marigo, Numerical experiments in revisited brittle fracture, Journal of the Mechanics and Physics of Solids 48 (2000) 797–826. doi:10.1016/S0022-5096(99)00028-9.

[7] H. Amor, J.-J. Marigo, C. Maurini, Regularized formulation of the variational brittle fracture with unilateral contact: Numerical experiments, Journal of the Mechanics and Physics of Solids 57 (2009) 1209–1229. doi:10.1016/j.jmps.2009.04.011.

[8] C. Miehe, M. Hofacker, F. Welschinger, A phase field model for rate-independent crack propagation: Robust algorithmic implementation based on operator splits, Computer Methods in Applied Mechanics and Engineering 199 (2010) 2765–2778. doi:10.1016/j.cma.2010.04.011.

[9] M. Ambati, T. Gerasimov, L. De Lorenzis, A review on phase-field models of brittle fracture and a new fast hybrid formulation, Computational Mechanics 55 (2015) 383–405. doi:10.1007/s00466-014-1109-y.

[10] J.-Y. Wu, A unified phase-field theory for the mechanics of damage and quasi-brittle failure, Journal of the Mechanics and Physics of Solids 103 (2017) 72–99. doi:10.1016/j.jmps.2017.03.015.

[11] S. Conti, M. Focardi, F. Iurlano, Phase field approximation of cohesive fracture models, Annales de l'Institut Henri Poincaré C, Analyse non linéaire 33 (2016) 1033–1067. doi:10.1016/j.anihpc.2015.02.001.

[12] G. Pijaudier-Cabot, Z. P. Bažant, Nonlocal damage theory, Journal of Engineering Mechanics 113 (1987) 1512–1533. doi:10.1061/(ASCE)0733-9399(1987)113:10(1512).

[13] R. H. J. Peerlings, R. de Borst, W. A. M. Brekelmans, J. H. P. de Vree, Gradient enhanced damage for quasi-brittle materials, International Journal for Numerical Methods in Engineering 39 (1996) 3391–3403. doi:10.1002/(SICI)1097-0207(19961015)39:19<3391::AID-NME7>3.0.CO;2-D.

[14] K. Pham, H. Amor, J.-J. Marigo, C. Maurini, Gradient damage models and their use to approximate brittle fracture, International Journal of Damage Mechanics 20 (2011) 618–652. doi:10.1177/1056789510386852.

[15] S. A. Silling, Reformulation of elasticity theory for discontinuities and long-range forces, Journal of the Mechanics and Physics of Solids 48 (2000) 175–209. doi:10.1016/S0022-5096(99)00029-0.

[16] R. Lipton, Cohesive dynamics and brittle fracture, Journal of Elasticity 124 (2016) 143–191. doi:10.1007/s10659-015-9564-z.

[17] H. Ren, T. Rabczuk, X. Zhuang, Variational damage model: A new paradigm for fractures, Frontiers of Structural and Civil Engineering 19 (2025) 1–21. doi:10.1007/s11709-025-1144-0.

[18] A. Braides, G. Dal Maso, Non-local approximation of the Mumford–Shah functional, Calculus of Variations and Partial Differential Equations 5 (1997) 293–322. doi:10.1007/s005260050068.

[19] L. Lussardi, M. Negri, Convergence of nonlocal finite element energies for fracture mechanics, Numerical Functional Analysis and Optimization 28 (2007) 83–109. doi:10.1080/01630560701189994.

[20] G. Scilla, F. Solombrino, Non-local approximation of the Griffith functional, NoDEA: Nonlinear Differential Equations and Applications 28 (2021) 17. doi:10.1007/s00030-021-00682-y.

[21] G. Dal Maso, Generalised functions of bounded deformation, Journal of the European Mathematical Society 15 (2013) 1943–1997. doi:10.4171/JEMS/410.

[22] F. Iurlano, A density result for GSBD and its application to the approximation of brittle fracture energies, Calculus of Variations and Partial Differential Equations 51 (2014) 315–342. doi:10.1007/s00526-013-0676-7.

[23] M. J. Borden, C. V. Verhoosel, M. A. Scott, T. J. R. Hughes, C. M. Landis, A phase-field description of dynamic brittle fracture, Computer Methods in Applied Mechanics and Engineering 217–220 (2012) 77–95. doi:10.1016/j.cma.2012.01.008.

[24] J. F. Kalthoff, Modes of dynamic shear failure in solids, International Journal of Fracture 101 (2000) 1–31. doi:10.1023/A:1007647800529.